Low-energy dissociative electron attachment to CF₂

S. T. Chourou,[1] Å. Larson,[2] and A. E. Orel[1]

[1]*University of California, Davis, Davis California 95616, USA*
[2]*Stockholm University, S-106 91 Stockholm, Sweden*

We present the results of a theoretical study of dissociative electron attachment (DEA) of low-energy electrons to CF₂. We carried out electron scattering calculations using the complex Kohn variational method at the static-exchange and relaxed self-consistent field (SCF) level at the equilibrium geometry and compare our differential cross sections to other results. We then repeated these calculations as a function of the three internal degrees of freedom to obtain the resonance energy surfaces and autoionization widths. We use this data as input to form the Hamiltonian relevant to the nuclear dynamics. The multidimensional wave equation is solved using the multiconfiguration time-dependent Hartree (MCTDH) approach within the local approximation.

I. INTRODUCTION

In the processing of semiconductor devices, fluorocarbon plasmas are often used to etch silicon surfaces [1,2]. The gases currently used in the plasma production of microelectronic devices have been shown to have a strong greenhouse effect. CF_3I and C_2F_4 have been proposed as alternate feedstock gases [3]. Although the feed gas is nonreactive, under electron bombardment it fragments to produce reactive species such as CF, CF_2, and CF_3 radicals and the corresponding ions. Electron collision cross sections for these transient, reactive species are difficult to measure experimentally. Therefore, *ab initio* theory can be of value in estimating the cross sections that are needed in large-scale simulations of these processing plasmas [4,5]. It is important to identify not only the cross sections but also the branching ratios into the various fragment channels following dissociation. These quantities are critical in modeling the behavior of the feedstock gases in a plasma environment [6].

One question that has arisen in these plasmas is the source of F^-. It had originally been predicted that dissociative electron attachment to C

$$CF + e^- \rightarrow (CF)^{-*} \rightarrow C + F^-$$

would be efficient [7,8]. Further calculations [9] showed that although, as found in the previous studies, the anion curve crossed the neutral near the equilibrium geometry, at the energies needed for dissociation [7,8] the cross section was extremely small and significant vibrational excitation was needed to produce any significant F^- product. It was also proposed that the dissociative electron attachment to CF_2

$$CF_2 + e^- \rightarrow (CF_2)^{-*} \rightarrow CF + F^-$$

might be efficient. *R*-matrix calculations were carried out at several internuclear separations, but no dynamics for the dissociation were calculated [8,10]. These calculations indicate the existence of at least one anion resonance $^2B_1$ ($^2A''$) which crosses the neutral and predicted the dissociative attachment cross section to be large. Later calculations [11] computed differential cross sections that compared well to experiments. These calculations at the static exchange level found a single resonance at low energy unbound at the equilibrium geometry of the ground state. However, when a static-exchange

plus polarization calculation was performed, which correctly balances the anion and target correlation, the anion was found to be bound. This is in agreement with photodetachment spectroscopy experiments [12] that found the CF_2^- anion to be bound. In addition, an experiment [13] which measured the cross section for the dissociative electron attachment to CF_2 found it to be no greater than $\sim 5 \times 10^{-20}$ cm². More recently [14], an experimental study of dissociative electron attachment to a number of fluorocarbon radicals found that the process yielded F^- with low efficiency (less than 2%), except in the case of CF_2, where no attachment was observed.

In this paper we present our calculations on the dissociative electron attachment to CF_2. We first describe the electron scattering calculations performed to determine the resonant states and construct the complex potential energy surfaces. We compare our differential electron scattering calculations with previous theoretical and experimental results. We discuss the computation of the nuclear dynamics of CF_2^{-*}. Finally, we present our results for the DEA cross section.

II. ELECTRON SCATTERING CALCULATIONS

We use the complex Kohn variational method [15] to describe the electron scattering from the neutral. This method has been described elsewhere so only a summary will be presented. The $(n + 1)$-electron scattering wave function for fixed nuclei positions represented collectively by the vector $\mathbf{Q}$ is written as

$$\Psi_{el}^\lambda(\mathbf{r}^{n+1}; \mathbf{Q}) = \hat{A}\left[\sum_{\lambda'}\phi_{el}^{\lambda'}(\mathbf{r}^n; \mathbf{Q})F^{\lambda\lambda'}(\vec{r}_{n+1}; k)\right]$$
$$+ \sum_\mu d_\mu^\lambda \Theta_\mu(\mathbf{r}^{n+1}; \mathbf{Q}), \qquad (1)$$

where $\mathbf{r}^{n+1} = (\vec{r}_1, \vec{r}_2, \ldots, \vec{r}_{n+1})$ is the $(n + 1)$-electronic coordinates vector and $\hat{A}$ is the antisymmetrizing operator. The first sum is denoted as the *P*-space portion of the wave function and runs over the energetically open target states. In this case, only one channel was open. The function $\phi_{el}^\lambda(\mathbf{r}^n; \mathbf{Q})$ is the target n-electron ground state in the irreducible representation λ with the nuclei clamped at $\mathbf{Q}$. The second term, denoted as the *Q*-space portion of the wave function, contains the
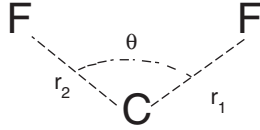
FIG. 1. Molecule in internal coordinates.

functions Θ_μ, which are square-integrable $n + 1$ configuration state functions (CSFs) which are used to describe short-range correlations and the effects of closed channels. $F^{\lambda\lambda'}(\vec{r}_{n+1}; k)$ is the scattering electron's wave function at position $\vec{r}$ and momentum k, which is further expanded to match asymptotic boundary conditions:

$$F^{\lambda\lambda'}(\vec{r}; k) = \sum_i c_i^{\lambda\lambda'} u_i(\vec{r}) + \sum_{lm} \left[f_l^\lambda(kr)\delta_{ll'}\delta_{mm'}\delta_{\lambda\lambda'} \right.$$
$$\left. + T_{ll'mm'}^{\lambda\lambda'}(k)h_l^{+\lambda}(kr) \right] Y_{lm}(\hat{r})/r, \qquad (2)$$

where the $\{u_i\}$ are square-integrable functions, $\{f_l^\lambda\}$ and $\{h_l^{+\lambda}\}$ are respectively the regular Ricatti-Bessel and the outgoing Hankel functions, and Y_{lm} are the normalized spherical harmonics. Angular momenta up to $l = 6$ and $|m| = 4$ are included in the calculation.

By inserting the trial wave function into the complex Kohn functional [15], the unknown coefficients in the trial wave function, d_μ^λ, $c_i^{\lambda\lambda'}$, and $T_{ll'mm'}^{\lambda\lambda'}$ can be optimized. The terms $T_{ll'mm'}^{\lambda\lambda'}$ are the T-matrix elements that determine the eigenphase sums as a function of the electron's collision energy. The eigenphase sums were fit to the Breit-Wigner form [16],

$$\delta\left(\frac{k^2}{2}\right) = \arctan\left(\frac{\Gamma/2}{\epsilon - \frac{k^2}{2}}\right) + \delta_{\text{bkgd}}\left(\frac{k^2}{2}\right), \qquad (3)$$

where ϵ, Γ are the corresponding parameters to be determined and δ_{bkgd} is the background phase shift taken to be a slowly varying function of the electron energy.

We performed calculations at two levels. In all calculations the carbon and flourine atoms were described using a triple-ζ-plus-polarization (TZP) function basis set [17], which is then augmented with one s with exponent 0.01 and one p function with exponent 0.09. The first calculation was carried out at the static exchange level. At this level a SCF wave function is used for the target wave function, $\phi_{\text{el}}^\lambda(\mathbf{r}^n; \mathbf{Q})$. In the second level of calculations, a static exchange plus polarization (SEP) calculation was run with a relaxed SCF (RSCF) wave function, that is, including all symmetry-preserving single excitations from the occupied target orbitals into all unoccupied orbitals. This has been used in previous studies [9] and found to yield a balanced description of the neutral and anion. This leads to 9075 configurations in $^2A''$, the symmetry that includes the resonance.

We have chosen to work in the internal coordinate system shown in Fig. 1. The coordinates r_1 and r_2 represent the distance between the two fluorine atoms and the carbon atom, and θ is the F-C-F angle.

A. Differential cross section

The fixed-nuclei differential cross section is computed and shown in Fig. 2 in comparison to experimental results and other
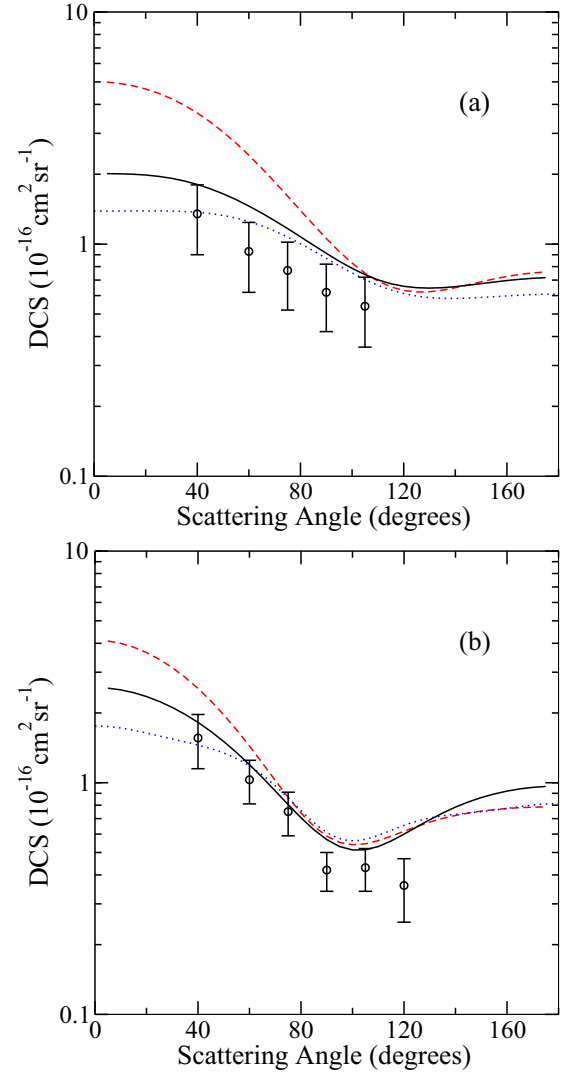

FIG. 2. (Color online) Differential cross section for electron scattering from CF_2 at (a) 3.0 and (b) 6.0 eV. The results at the static exchange level are shown with dashed lines (red online), while the solid black lines show the results at the RSCF level. Results from previous calculations [11] and experiments [11] are displayed with the dotted (blue online) lines and symbols respectively.

calculations. In order to compare to the previous calculations, our results are shown without the Born correction. Since the experiment could not be performed below $20°$ and the effect of the dipole moment will become significant below $10°$ the differential cross sections plotted should be reliable. As can been seen in the figure, there is very good agreement between the two calculations and the experimental results. The static exchange results of the previous calculation [11] and our static exchange calculations cannot be distinguished on the figure, so only ours are shown. Adding polarization to the calculation lowers the cross section in the forward direction. As the energy increases the effect of polarization decreases. The differences between the two calculations and the experiment may be due to changes in the differential cross section as a function of nuclear geometry. The calculations shown are at fixed geometry. These results should be averaged over the initial target vibrational
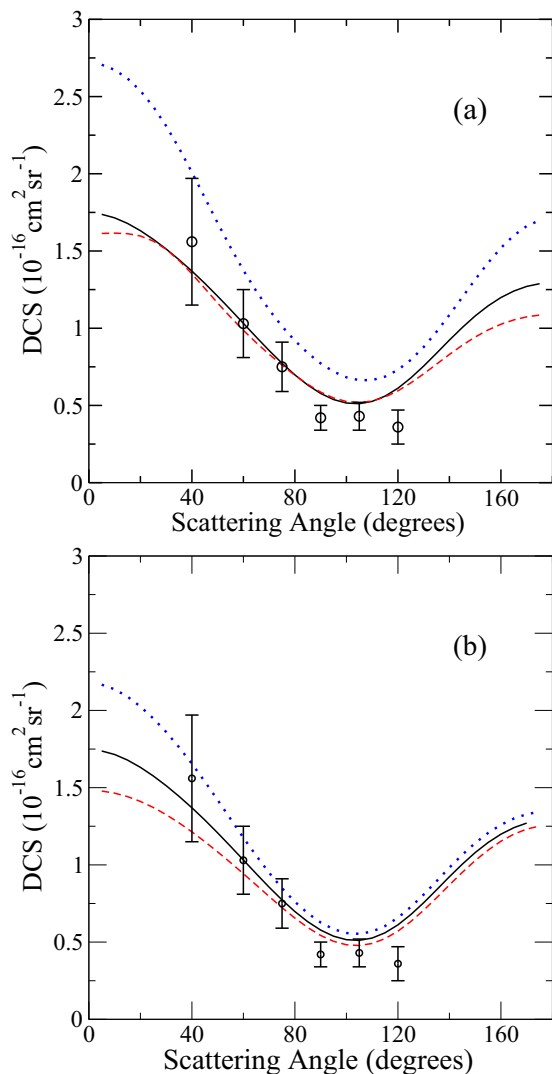
FIG. 3. (Color online) (a) Effect of changing the C-F bond distance on the differential cross section $\theta = 104.8°$, one C-F bond fixed at $r_1 = 2.4$ a_0 and the second at $r_2 = 2.3$ a_0, dashed line (red online); $r_2 = 2.4$ a_0, solid black line; and $r_2 = 2.6$ a_0, dotted line (blue online). (b) Molecule bending effect on the differential cross section for $r_2 = 2.4$ a_0 and angle θ fixed at 100°, dashed line (red online); 104.8°, solid black line; and 110°, dotted line (blue online).

FIG. 4. (Color online) (a) Effect of changing the C-F bond distance on the eigenphase sum θ fixed at 104.8° and one C-F bond fixed at $r_1 = 2.4$ a_0 and $r_2 = 1.4$ a_0, black solid line; $r_2 = 1.6$ a_0, dotted line (red online); $r_2 = 1.8$ a_0, dashed line (green online); $r_2 = 2.0$ a_0, dot-dashed (blue online); and $r_2 = 2.3$ a_0, dot-dot-dashed (magenta online). (b) Molecule bending effect on the eigenphase sums for $r_1 = r_2 = 2.0$ a_0 and angle θ fixed at 90°, dashed line (red online); 104.8°, solid black line; and 120°, dotted line (blue online).

wave function. The effect is usually small, but in this case the resonance becomes bound in the Franck-Condon region. In order to see the magnitude of the change we repeated these calculations for a range of angles and bond distances. Figure 3 shows the effect of changes in these parameters. As can be seen, the cross section in the forward direction is quite sensitive to changes in the internuclear separation and the bend. These results show that the relaxed SCF calculation gives a good description of the electron scattering in the low-energy region. Therefore, the calculations of the resonant surfaces were done at this level.

B. Resonance surface

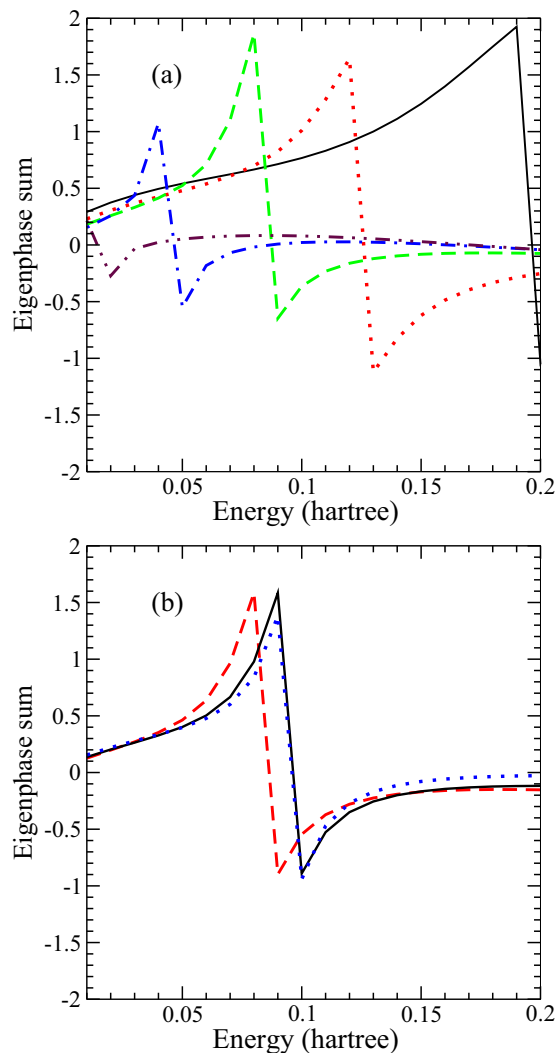The computation of the eigenphase sums as a function of incident electron energy reveals one low-lying shape resonance. In Fig. 4 the eigenphase sum show the resonance feature of CF_2 in $^2A''$ symmetry up to an electron collision energy of 0.2 Hartrees (5.44 eV). Figure 4(a) displays the effect of changing the C-F bond, while keeping the angle fixed at the equilibrium geometry, $\theta = 104.8°$, and the other C-F bond at 2.4 a_0. As can been seen in the figure, the resonance moves to lower energy and becomes bound as the bond distance is increased. Figure 4(b) shows the effect of bending at fixed bond distances. The eigenphase sums shown in the figure were calculated at the bond distances fixed at $r_1 = r_2 = 2.0$ a_0, where the resonance is not bound. As can be seen in the figure, the resonance energy position is much less sensitive to the bend angle. The potential energy used in our calculations is expressed in the (r_1, r_2, θ) coordinates spanning the domain $[1.6\ a_0, 8.0\ a_0] \times [1.6\ a_0, 8.0\ a_0] \times [80°, 160°]$.
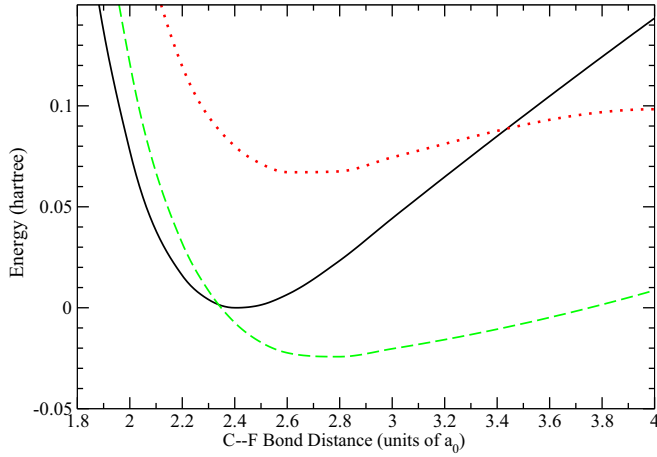
FIG. 5. (Color online) One-dimensional cut of the potential energy surfaces of the ground state of the neutral CF_2, solid black line, and the ground state of the anion CF_2^- at the static-exchange level, dotted line (red online), and the relaxed SCF level, dashed line (green online), as a function of r_2 with r_1 fixed at 2.4 a_0 and the angle θ fixed at 104.8°.

For comparison, a one-dimensional cut of the potential energy surfaces of the ground state of the neutral CF_2 and the anion CF_2^- at the static-exchange level and the RSCF level are shown in Fig. 5 as a function of r_2 with r_1 fixed at 2.4 a_0 and the angle θ fixed at 104.8°. The dissociation energy for the ground state is found to be 0.25 Hartrees (6.8 eV) in fair agreement with the measured value in Ref. [18]. The anion surface at the RSCF crosses the neutral at a bond distance smaller than the equilibrium bond distance of the neutral.

The potential energy surfaces of both the ground state of the neutral and anion molecules show little changes when the angle is varied. One-dimensional cuts for several angles are shown in Fig. 6(a) for the neutral and Fig. 6(b) for the anion at the RSCF level as a function of r_2 with r_1 fixed at 2.4a_0. There is a much stronger variation with change in the bond distance. One-dimensional cuts for several values of r_1 are shown in Fig. 7(a) for the neutral and Fig. 7(b) for the anion at the RSCF level with the angle θ fixed at 104.8°.

Similar behavior is seen for the autoionization width, shown in Fig. 8. There is little variation with angle, but a stronger change with internuclear separation.

III. NUCLEAR DYNAMICS

We solve for the nuclear dynamics of the metastable negative-ion state in the local complex potential model. The approximation used in this model has been discussed in detail elsewhere [19] and will only be outlined here. The nuclear wave equation is given by

$$[E_{\text{tot}} - \hat{H}(\mathbf{Q})]\xi_\nu(\mathbf{Q}) = \eta_\nu(\mathbf{Q}), \tag{4}$$

where the Hamiltonian operator is given by

$$\hat{H}(\mathbf{Q}) = \hat{T}_Q + V_{\text{el}}(\mathbf{Q}). \tag{5}$$

The kinetic energy operator $\hat{T}_Q$ for a total momentum operator $J = 0$ is given in the (r_1, r_2, θ) coordinate system
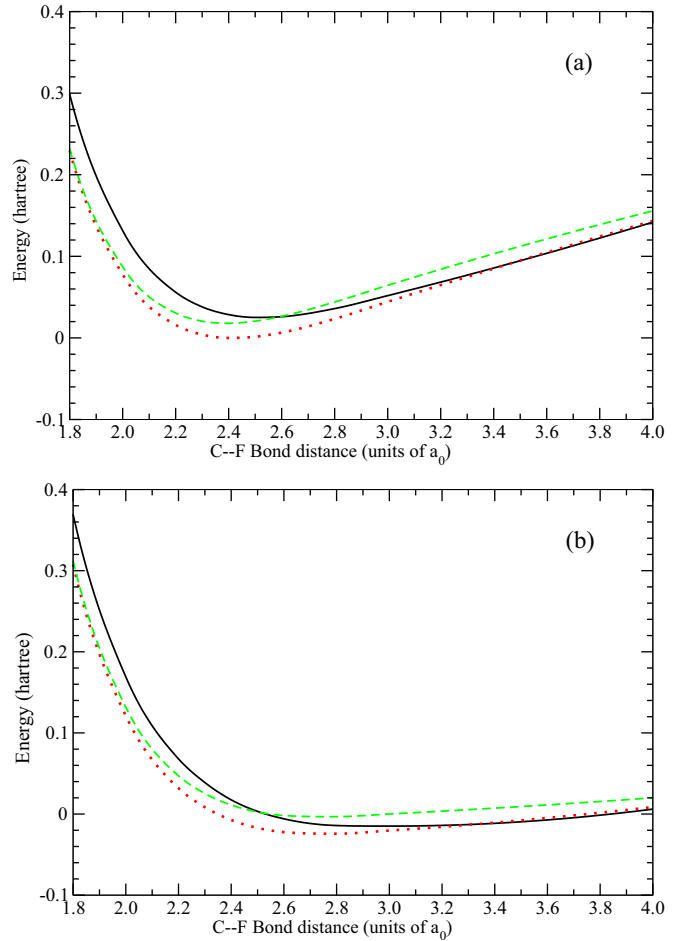

FIG. 6. (Color online) Potential energy surfaces of the ground state of the neutral CF_2 (a) and the anion CF_2^- (b) as a function of r_2, r_1 fixed at 2.4 a_0 for three values of θ: 90.0°, black solid line; 104.8°, dotted line (red online); and 120.0°, dashed line (green online).

by

$$\hat{T}_Q = -\frac{1}{2\mu_1}\partial_{r_1}^2 - \frac{1}{2\mu_2}\partial_{r_2}^2 + \left(\frac{1}{2\mu_1 r_1^2} + \frac{1}{2\mu_2 r_2^2}\right)\hat{j}^2$$
$$- \frac{1}{2m_C}\partial_{r_1}\partial_{r_2} + \frac{1}{m_C}\left(\frac{1}{r_1}\partial_{r_2} + \frac{1}{r_2}\partial_{r_1}\right)\partial_\theta \sin(\theta)$$
$$- \frac{1}{2m_C r_1 r_2}[\cos(\theta)\hat{j}^2 + \hat{j}^2\cos(\theta)], \tag{6}$$

where $\mu_1 = \mu_2 = (\frac{1}{m_F} + \frac{1}{m_C})^{-1}$ defines the reduced masses associated with r_1 and r_2 with m_C and m_F being the masses of the carbon and fluoride atoms respectively. The operator $\hat{j}^2$ in Eq. (6) represents the angular momentum operator squared. (Note that we use atomic units $\hbar = m_e = 1$ throughout.) The complex potential $V_{\text{el}}(\mathbf{Q})$ relevant to the resonant CF_2^- anion is defined by

$$V_{\text{el}}(\mathbf{Q}) = E_{\text{el}}(\mathbf{Q}) + \epsilon_{\text{res}}(\mathbf{Q}) - \frac{i}{2}\Gamma(\mathbf{Q}). \tag{7}$$

The driving term $\eta_\nu(\mathbf{Q})$ in Eq. (4) is known as the entry amplitude and it expresses the capture probability of the incoming electron by the molecular target in the discrete
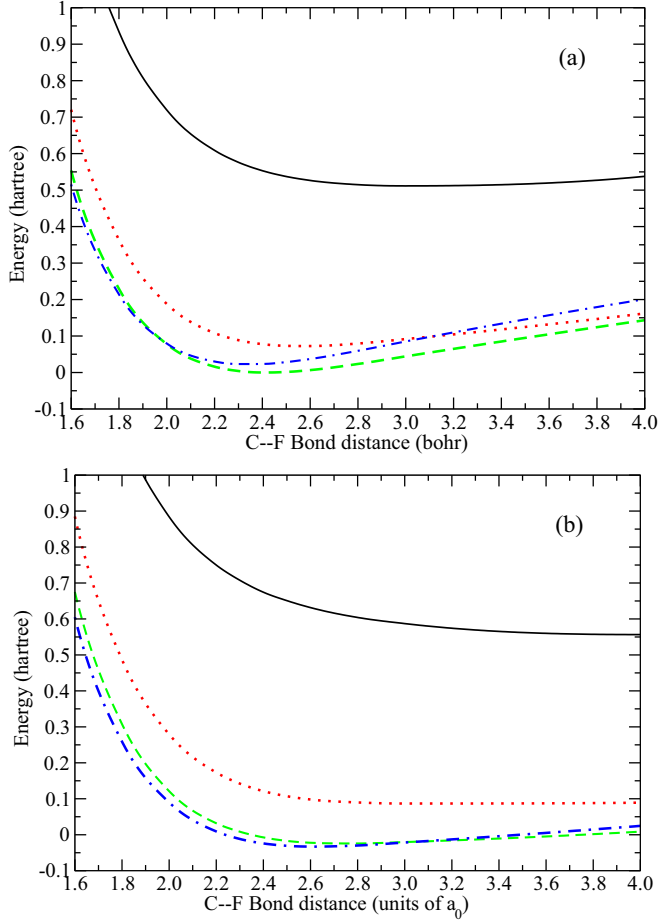
FIG. 7. (Color online) Potential energy surfaces of the ground state of the neutral CF_2 (a) and the anion CF_2^- (b) as a function of r_2, θ fixed at 104.8° for four values of r_1: 1.6 a_0, black solid line; 1.8 a_0, dotted line (red online); 2.4 a_0, dashed line (green online); and 2.8 a_0, dash-dotted line (blue online).

vibrational state $\chi_\nu(\mathbf{Q})$ into the resonant state associated with the complex potential of Eq. (7). In our model, it is expressed as

$$\eta_\nu(\mathbf{Q}) = \left(\frac{\Gamma(\mathbf{Q})}{2\pi}\right)^{1/2}\chi_\nu(\mathbf{Q}). \tag{8}$$

Finally, $\xi_\nu(\mathbf{Q})$ is the nuclear wave function we seek to determine. We use the time-dependent formulation established by McCurdy and Turner [20]. The problem thus reduces to solving the time-dependent Schrödinger equation:

$$\hat{H}(\mathbf{Q})\Phi_{\text{nuc}}(\mathbf{Q},t) = i\,\partial_t\Phi_{\text{nuc}}(\mathbf{Q},t);$$
$$\Phi_{\text{nuc}}(\mathbf{Q},0) = \eta_\nu(\mathbf{Q}). \tag{9}$$

We use the computational technique based on multiconfiguration time-dependent Hartree (MCTDH) formalism discussed in detail in Ref. [21]. In the context of this theory, the nuclear wave function for the negative ion of CF_2 is expressed in the internal coordinates as

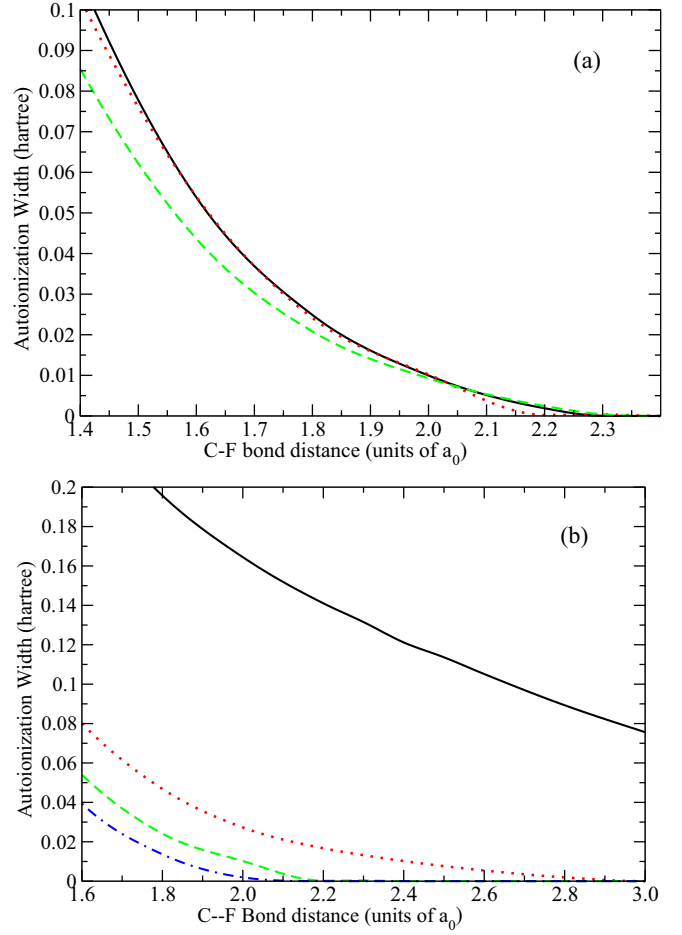$$\Phi_{\text{nuc}}(r_1,r_2,\theta,t) = \sum_{i,j,k}^{N_r,N_r,N_\theta} A_{ijk}(t)w_{i,j,k}(r_1,r_2,\theta,t), \tag{10}$$

FIG. 8. (Color online) Autoionization width (a) as a function of r_2, r_1 fixed at 2.4 a_0 for three values of θ: 90.0 °, black solid line; 104.8°, dotted line (red online); and 120.0°, dashed line (green online); and (b) as a function of r_2, θ fixed at 104.8° for four values of r_1: black solid line, 1.6 a_0; dotted line (red online), 1.8 a_0; dashed line (green online), 2.4 a_0; and dash-dotted line (blue online), 2.8 a_0.

where

$$w_{i,j,k}(r_1,r_2,\theta,t) = \rho_i^1(r_1,t)\rho_j^2(r_2,t)\Theta_k(\theta,t). \tag{11}$$

Each single-particle function appearing in Eq. (11) is in turn expanded in terms of a function basis set chosen to correspond to that of a discrete variable representation (DVR) for computational efficiency. Here, $N_{r_1} = N_{r_2} = 30$ and $N_\theta = 8$. The single-particle functions associated with the variables r_1 and r_2 are expressed in terms of sine-DVR (300 grid points each) and the angle θ is represented by the Legendre-DVR (66 grid points).

IV. COMPUTATIONAL RESULTS

The wave packet for the ground neutral state is computed by relaxation, that is, propagation on the neutral adiabatic potential energy surface in negative imaginary time. By applying Eq. (8), we determine the initial wave packet needed to solve the system of equation Eq. (9).

At the grid boundaries, an appropriate complex absorbing potential (CAP) is included to ensure that wave packet is not

reflected back into the grid, causing undesired interferences. The form of the CAPs adopted in this study is given by the form

$$-iW(R) = -iC|R - R_{\text{CAP}}|^b S(R - R_{\text{CAP}}), \quad (12)$$

where S is the Heaviside step function and the values of the parameters C, b, and R_{CAP} used in this propagation are 0.01, 3.0, and 5.0 a_0, respectively. Propagation is carried out for a duration of 1000 fs.

A. Cross section

The wave-packet flux at the grid boundaries is used to compute the DEA cross section. The energy-resolved outgoing flux associated with the initial target vibrational state ν through the CAP is therefore given by

$$F_\nu(E) = \frac{1}{(2\pi)^2|\Delta(E)|^2}\langle\xi_\nu|\widehat{F}|\xi_\nu\rangle_{\mathbf{Q}}, \quad (13)$$

where $\widehat{F}$ is the flux operator and $\Delta(E)$ is the energy distribution of the initial wave packet [22]. In order to achieve a time-dependent dynamics formulation of the process, the bracket term in Eq. (13) is computed in terms of the time domain integrals as

$$\langle\xi_\nu|\widehat{F}|\xi_\nu\rangle_{\mathbf{Q}} = \int_0^\infty dt \int_0^\infty dt'$$

$$\times \langle\eta_\nu|e^{i(\widehat{H}^\dagger-E)t}\widehat{F}e^{-i(\widehat{H}-E)t'}|\eta_\nu\rangle_{\mathbf{Q}}, \quad (14)$$

where the operator $\widehat{\widetilde{H}}$ is given by

$$\widehat{\widetilde{H}} = \widehat{H} - iW(R), \quad (15)$$

representing the CAP-perturbed Hamiltonian of the system defined in Eq. (5).

The cross section relevant to the DEA channel for an initial neutral target in the vibrational mode ν may be expressed based on the flux function as

$$\sigma_{\nu\to\text{DEA}}\left(\frac{k^2}{2}\right) = g_s g_a \frac{4\pi^3}{k^2} F_\nu\left(\frac{k^2}{2}\right), \quad (16)$$

where g_s is the statistical ratio of the resonant state to the ionization continuum (here equal to 1) and g_a is the arrangement multiplicity (here equal to 2). The reader is referred to Refs. [22–25] for detailed treatment of the CAP-based flux formalism.

In Fig. 9, the DEA cross section at the RSCF level is shown for one-dimensional (θ and one C-F bond fixed), two-dimensional (θ fixed), and three-dimensional calculations. In the one-dimensional (1D) calculation, the electron can be captured at low collision energy; however, the anion state is not open for dissociation until the energy is larger than 2 eV. It is the high-energy tail of the capture probability that has enough energy for dissociation. The cross section calculated within the 1D model is very small (10^{-21} cm^2) with regular oscillations due to energy-dependent overlap between the vibrational wave function of the target molecular and the continuum function of the anion [26,27]. In two dimensions, the peak of the cross section occurs around 3 eV and with a peak height of roughly 1×10^{-19} cm^2. However, when the bend is added the cross section drops. Bending does not lead to dissociation, so as the
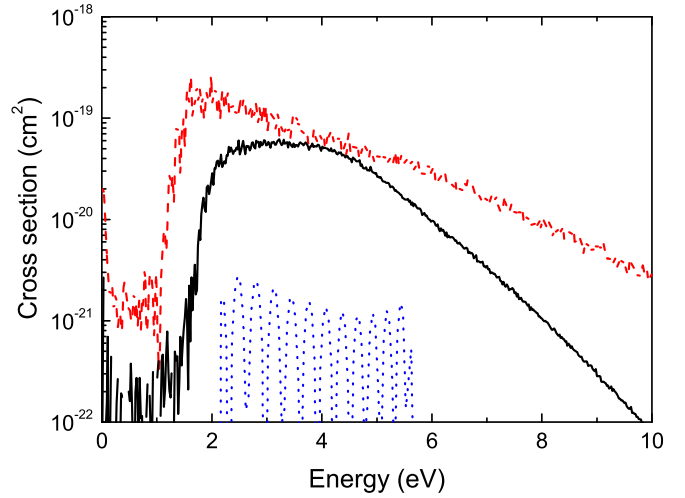

FIG. 9. (Color online) DEA cross section for F$^-$ production from CF$_2$ with resonance parameters determined at the RSCF level: one-dimensional, dotted line (blue online) with r_1 as variable and θ and r_2 fixed; dashed line (red online), two-dimensional surface with r_1 and r_2 as variables and θ fixed; and black solid line, full three-dimensional surface.

wave packet spreads in that dimension it can only autoionize. We obtain a peak value of 6×10^{-20} cm^2 at around 2 eV. This is consistent with the estimate given by Graupner *et al.* [13], which put an upper limit on the DEA cross section of less than 5×10^{-20} cm^2 for energies less than 10 eV and the observations of Shuman *et al.* [14] that observed no attachment in this system over a similar energy range.

In the experiments [13] the temperature was 300 K. The vibrational frequencies are as follows: symmetric stretch, 152 meV; asymmetric stretch, 138 meV; and bend, 82 meV [28]. Therefore the symmetric and asymmetric stretches are in the ground vibrational states. The lower
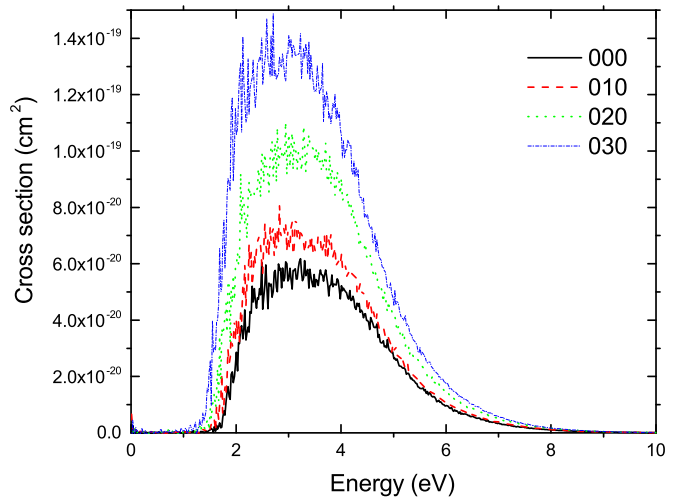

FIG. 10. (Color online) DEA cross section for F$^-$ production from CF$_2$ as a function of initial vibrational excitation in the bending mode: $\nu = 0$, solid line (black online); $\nu = 1$, dashed line (red online); $\nu = 2$, dotted line (green online); and $\nu = 3$, dot-dashed line (blue online).

frequency bend has a population of 4% in $\nu = 1$ and 96% in $\nu = 0$. In order to assess the effect of vibrational excitation, a calculation was carried out with excitation in the bend. The results are shown in Fig. 10. The cross section increases with increasing vibrational excitation, but by $\nu = 3$ it is only a factor of ten higher. This will not lead to any significant changes the dissociative electron attachment rate.

V. CONCLUSION

We have carried out theoretical calculations on DEA of CF_2. These calculations show that the resonance that appears at the static-exchange calculations at the equilibrium geometry becomes bound when polarization effects are included. The DEA cross section is found to be quite small, in agreement with the most recent experiments. This means, as previously speculated [8,10], that DEA of CF_2, as was found with our previous studies of DEA of CF, cannot be a source of F^- in processing plasmas. Further work is needed to study, for example, DEA of CF_3 to see if this system could be a source, although recent experiments [14] indicate this is inefficient. Another possible source is the ion-pair channel in the dissociative recombination of CF^+, with the process

$$CF^+ + e^- \rightarrow C^+ + F^-.$$
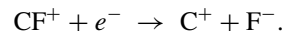
Further work is needed to test this possibility.

[1] L. G. Christophorou and J. K. Olthoff, Appl. Surf. Sci. **192**, 309 (2002).

[2] L. G. Christophorou and J. K. Olthoff, *Fundamental Electron Interactions with Plasma Processing Gases* (Kluwer Academic, New York, 2004).

[3] S. Samukawa, T. Mukai, and Noguchi, Mater. Sci. Semcond. Process **2**, 203 (1999).

[4] V. Georgieva, A. Bogaerts, and R. Gijbels, J. Appl. Phys. **94**, 3748 (2003).

[5] K. Denpoh and K. Nambu, Jpn. J. Appl. Phys. **39**, 2804 (2000).

[6] M. J. Kushner, *Database Needs for Modeling and Simulation of Plasma Processing* (National Research Council, Washington, DC, 1996).

[7] I. Rozum, N. J. Mason, and J. Tennyson, J. Phys. B **35**, 1583 (2002).

[8] I. Rozum, P. Limão-Vieira, S. Eden, J. Tennyson, and N. J. Mason, Phys. Chem. Ref. Data **35**, 267 (2006).

[9] C. S. Trevisan, A. E. Orel, and T. N. Rescigno, Phys. Rev. A **72**, 062720 (2005).

[10] I. Rozum and J. Tennyson, J. Phys. B **37**, 957 (2004).

[11] J. R. Francis-Staite, T. M. Maddern, M. J. Brunger, S. J. Buckman, C. Winstead, V. McKoy, M. A. Bolorizadeh, and H. Cho, Phys. Rev. A **79**, 052705 (2009).

[12] R. L. Schwartz, G. E. Davico, T. M. Ramond, and W. C. Lindberger, J. Phys. Chem. **103**, 8213 (1999).

[13] K. Graupner, T. Field, and C. A. Mayhew, New J. Phys. **12**, 083035 (2010).

[14] N. S. Shuman, T. M. Miller, and A. A. Viggiano, J. Chem. Phys. **137**, 214318 (2012).

[15] T. N. Rescigno, B. H. Lengsfield, and C. W. McCurdy, in *Modern Electronic Structure Theory*, edited by D. R. Yarkony (World Scientific, Singapore, 1995), Vol. 1, p. 501.

[16] S. Geltman, *Topics in Atomic Collision Theory* (Krieger Publishing company, Malabar, 1997), p. 31.

[17] T. H. Dunning Jr. and P. J. Hay, in *Methods of Electronic Structure Theory*, edited by H. F. Schaefer III (Plenum Press, New York, 1977), pp. 1–27.

[18] M. W. Chase, Jr., C. A. Davies, J. R. Downey, Jr., D. J. Frurip, R. A. McDonald, and A. N. Syverud, *JANAF Thermochemical Tables*, 3rd ed., J. Phys. Chem. Ref. Data, Vol. 14, Suppl. 1 (1985), http://www.nist.gov/data/PDFfiles/jpcrdS1V14.pdf.

[19] T. F. O'Malley, Phys. Rev. **150**, 14 (1966).

[20] C. W. McCurdy and J. L. Turner, J. Chem. Phys. **78**, 6773 (1983).

[21] G. A. Worth, M. H. Beck, A. Jäckle, and H.-D. Meyer, MCTDH package, version 8.4 (2007); see http://www.pci.uni-heidelberg.de/tc/usr/mctdh/

[22] A. Jäckle and H.-D. Meyer, J. Chem. Phys. **105**, 6778 (1996).

[23] M. H. Beck, A. Jäckle, G. A. Worth, and H.-D. Meyer, Phys. Rep. **324**, 1 (2000).

[24] H.-D. Meyer and G. A. Worth, Theor. Chem. Acc. **109**, 251 (2003).

[25] U. V. Riss and H.-D. Meyer, Phys. B: At. Mol. Opt. Phys. **26**, 4503 (1993).

[26] O. Motapon, M. Fifirig, A. Florescu, F. O. Waffeu Tamo, O. Crumeyrolle, G. Varin-Bréant, A. Bultel, P. Vervisch, J. Tennyson, and I. F. Schneider, Plasma Sources Sci. Technol. **15**, 23 (2006).

[27] J. B. Roos, Å. Larson, and A. E. Orel, Phys. Rev. A **78**, 022508 (2008).

[28] H. B. Qian and P. B. Davies, J. Mol. Spectrosc. **169**, 201 (1995).